frontiers | Frontiers in Physics

TYPE Original Research
PUBLISHED 29 August 2025
DOI 10.3389/fphy.2025.1641031

OPEN ACCESS

EDITED BY
Imran Khan,
COMSATS Institute of Information Technology, Pakistan

REVIEWED BY
Peican Zhu,
Northwestern Polytechnical University, China
Kemal Gokhan Nalbant,
Beykent University, Türkiye
Halimjon Khujamatov,
Tashkent University of Information Technology, Uzbekistan

*CORRESPONDENCE
Rozalina Zakaria,
rozalinaa@um.edu.my
Roosvel Soto-Diaz,
roosvel.soto@unsimon.edu.co
Darius Andriukaitis,
darius.andrikatis@ktu.lt

RECEIVED 04 June 2025
ACCEPTED 30 July 2025
PUBLISHED 29 August 2025

CITATION
Mohamed HG, Kilius S, Zakaria R, Soto-Diaz R, Escorcia-Gutierrez J and Andriukaitis D (2025) Novel chiral metasurface design with ring resonators for THz applications.
Front. Phys. 13:1641031.
doi: 10.3389/fphy.2025.1641031

Novel chiral metasurface design with ring resonators for THz applications

Heba G. Mohamed[1], Sarunas Kilius[2], Rozalina Zakaria[3]*, Roosvel Soto-Diaz[4]*, José Escorcia-Gutierrez[5] and Darius Andriukaitis[2]*

[1]Department of Electrical Engineering, College of Engineering, Princess Nourah bint Abdulrahman University, Riyadh, Saudi Arabia, [2]Department of Electronics Engineering, Faculty of Electrical and Electronics Engineering, Kaunas University of Technology, Kaunas, Lithuania, [3]Photonics Research Centre, University of Malaya, Kuala Lumpur, Malaysia, [4]Biomedical Engineering Program, Universidad Simón Bolívar, Barranquilla, Colombia, [5]Department of Computational Science and Electronics, Universidad de la Costa, CUC, Barranquilla, Colombia

Introduction: As an artificial two-dimensional material, metasurfaces are essential for modifying the fundamental characteristics of electromagnetic (EM) waves. Numerous researchers have created and validated metasurface uses, including anomalous reflection, polarization rotation, and absorption. The development of chiral metasurfaces that exhibit spin-selective transmission or reflection offers a novel method of manipulating circularly polarized (CP) waves. Because of their enormous chiroptical responses, which are orders of magnitude larger than those of natural chiral materials, chiral metasurfaces have also garnered a lot of interest in the field of spin photonics.

Methods: This paper proposes a novel chiral metasurface for dual-band THz circularly polarized anomalous reflecting and absorbing. The co-polarized reflection for incident right-handed and lefthanded circularly polarized waves is achieved via the metasurface structure, which is made up of two chiral structures. The corresponding absorption rates are 96.3% and 90.9%, respectively. The full 360° coverage is realized by rotating the chiral metasurface unit using Pancharatnam-Berry phase principle.

Results and Discussion: Simulation results show that the proposed metasurface has multi-function beam control capability and can be deployed in chiral sensing, electromagnetic energy harvesting, polarization converters, radar and other applications.

KEYWORDS

metasurface, THz waves, metamaterial absorber, dual-polarized beam control, circular polarization

1 Introduction

Electronic waves with a frequency range of 0.1~10 THz are known as terahertz (THz) waves. These waves have a wide range of potential uses in non-destructive testing, security monitoring, 6G communications, and space situational awareness [1]. THz waves fall in between photonics and electronics. There is a "terahertz gap" in the electromagnetic spectrum as a result of the limited development of THz functional

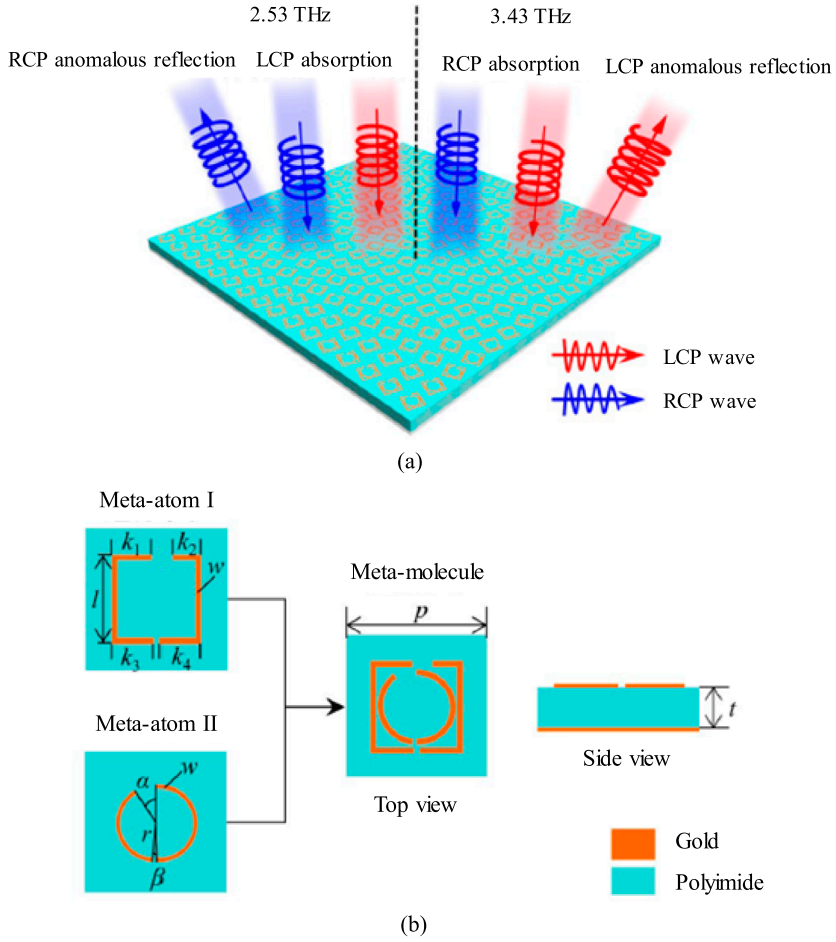

FIGURE 1
Schematic diagram of the function and unit structure of chiral metasurface array. **(a)** Metasurface array function **(b)** Metasurface unit structure.

devices caused by the difficulty of producing efficient THz responses in natural materials [2, 3]. Metasurfaces are two-dimensional metamaterials that are made by arranging sub-wavelength artificial electromagnetic structural units in a certain pattern. They have unique electromagnetic property control capabilities for electromagnetic waves [4] and can achieve a variety of electromagnetic control functions such as wave absorption [5–7], superlenses [8, 9], asymmetric transmission [10, 11], polarization conversion [12], vortex waves [13]. The cross-integration of metamaterials and THz frequency provides an important way to solve the bottleneck of conventional THz technology. A common geometric feature found in structures like proteins and DNA double helix molecules is chirality [14]. In the electromagnetic environment, chiral structures can generate circular dichroism (CD) [15] and circular birefringence optical rotation effects [16], as well as distinct reactions to left-handed circularly polarized (LCP) and right-handed circularly polarized (RCP) electromagnetic waves. Artificially designed metamaterials/metasurfaces can achieve chiral effects far greater than those of natural materials [17]. Chiral metamaterials/metasurfaces have been applied in electromagnetic wave amplitude and phase regulation and

TABLE 1 Metasurface unit parameters.

Parameter	Value
p	33.5 μ m
w	1.2 μ m
l	21 μ m
k_1	9 μ m
k_2	5.5 μ m
k_3	10 μ m
k_4	10 μ m
r	9 μ m
α	30°
β	5°
t	10.5 μ m

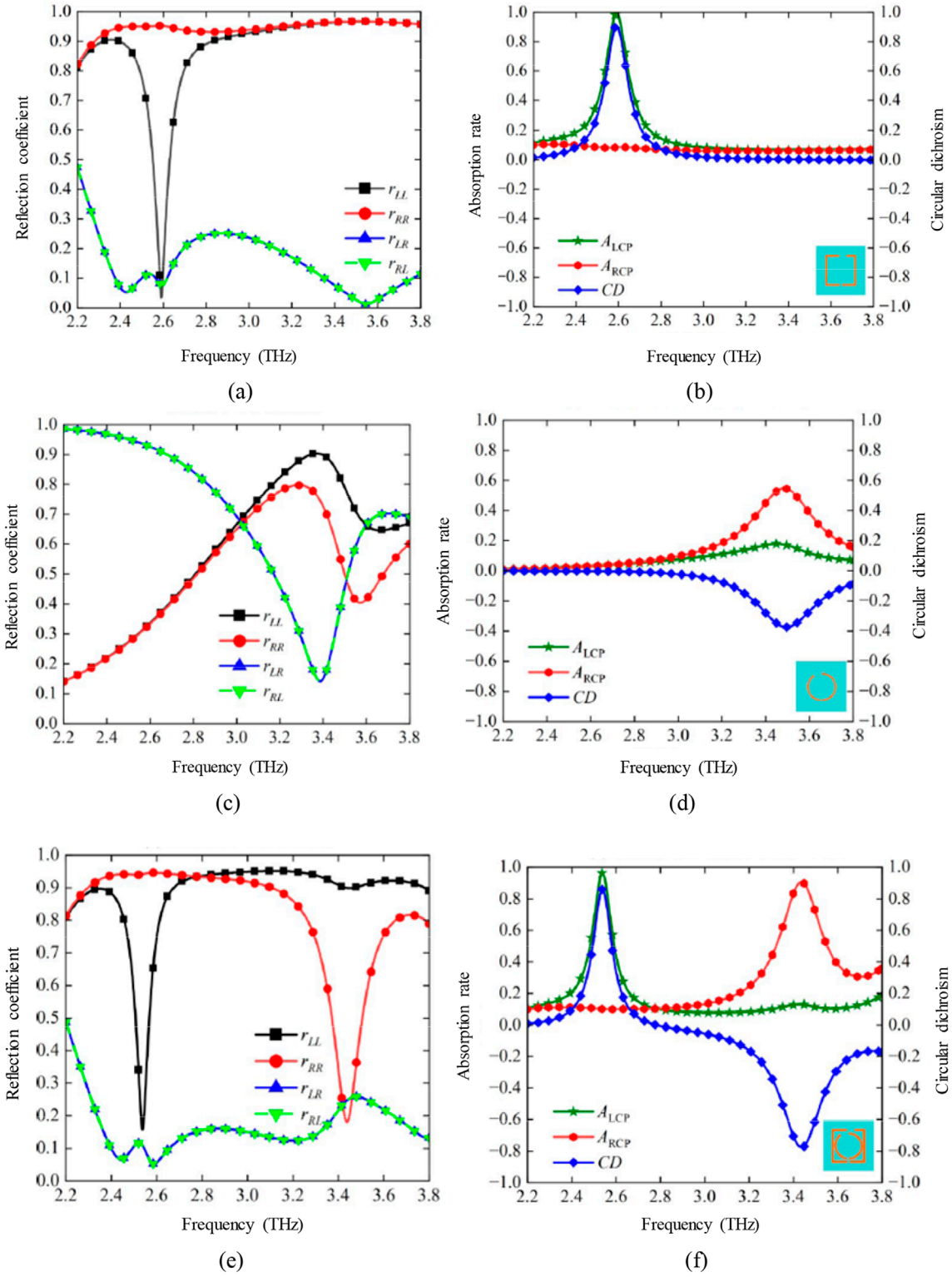

FIGURE 2
Simulation results of unit reflectance, absorptivity and circular dichroism. **(a)** Meta-atom I reflection coefficient **(b)** Meta-atom I absorption and circular dichoism **(c)** Meta-atom II reflection coefficient **(d)** Meta-atom II absorption and circular dichoism **(e)** Meta-molecule reflection coefficient **(f)** Meta-molecule absorption and circular dichoism.

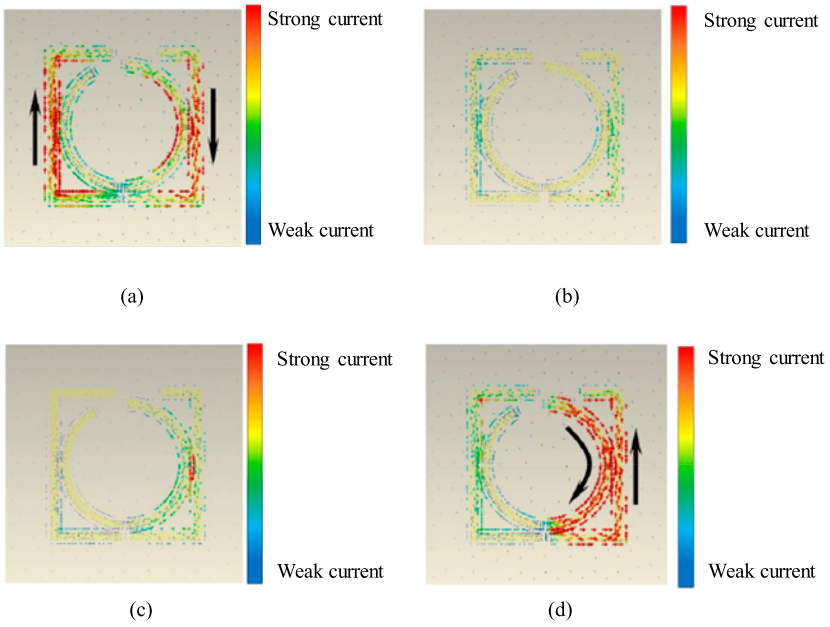

FIGURE 3
Current distribution on the surface of meta-molecular unit. **(a)** 2.53 THz LCP normal incidence **(b)** 2.53 THz RCP normal incidence **(c)** 3.43 THz LCP normal incidence **(d)** 3.43 THz RCP normal incidence.

polarization conversion. Some scholars have proposed using chiral metasurfaces to absorb circularly polarized waves [18]. When LCP/RCP waves are incident on chiral metasurfaces, only one type of electromagnetic wave is efficiently absorbed. Reflecting or transmitting orthogonally polarized electromagnetic waves exhibits circular dichroism [19–22]. The authors in [23] proposed the generalized Snell's law, which laid a theoretical foundation for the design of phase-controlled metasurfaces. Through resonant phase units [24] and geometric (Pancharatnam-Berry) phase units [25], electromagnetic control of abnormal reflection and abnormal refraction of electromagnetic waves can be achieved. Among them, geometric phase is an important means for metasurfaces to control THz circularly polarized waves. By rotating the unit, the reflected or transmitted circularly polarized wave can produce a phase difference of two times the rotation angle, thereby achieving abnormal reflection or transmission of circularly polarized waves [26, 27].

The authors in [28] proposed using a V-shaped unit structure to form a single-layer new artificial electromagnetic surface. By changing the angle of the V-shaped unit structure, the phase wavefront of the electromagnetic wave can be controlled to generate a vortex beam. The authors in [29] proposed a metasurface based on graphene materials. By changing the chemical potential of the graphene unit, a modally tunable OAM beam can be achieved in the range of 4.2–5.6 THz. The authors in [30] proposed a metasurface based on VO_2 materials. By driving the change from the insulating state to the metallic state of VO_2 by temperature change, an OAM beam with reconfigurable modes and beam steering angle can be achieved in the range of 0.69–0.79 THz. In [31], the research group further proposed to use VO_2 to convert THz incident waves into outgoing beams with different modes or frequencies in a tunable THz operating frequency band. The authors in [32] used the temperature control properties of InSb materials and based on the geometric phase principle to produce a modally reconfigurable metasurface in the frequency range of 1.8–4.5 THz.

At present, the design of THz chiral metasurfaces is mainly for a single function or a single frequency band, and the research on THz multi-band multifunctional chiral metasurfaces needs to be deepened.

This paper proposes a novel dual-frequency THz wave absorbing and anomalous reflecting circular-polarized chiral metasurface. The main contributions are as follows.

1) This metasurface can adjust the amplitude and phase of circularly polarized waves according to their rotation direction, and realize the dual-function integration of circularly polarized wave absorbing and abnormal reflection.
2) It can absorb the incident wave of LCP at a low frequency of 2.53 THz, and abnormally reflect the incident wave of RCP at an angle of −26° and maintain its chirality.
3) It absorbs the incident wave of RCP at high frequency of 3.43 THz, and abnormally reflects the incident wave of LCP at an angle of +19° and maintains its chirality.
4) The metasurface array designed in this paper has a simple structure and is easy to integrate.
5) It has great application potential in the fields of THz electromagnetic energy collection, polarization converters, chiral sensing, radar, etc.

The remainder of this paper is organized as follows. In Section 2, the theoretical analysis of the metasurface is performed. In Section 3, the absorption performance is evaluated. In Section 4, the metasurface array design and performance is discussed. In Section 5, the conclusion is discussed.

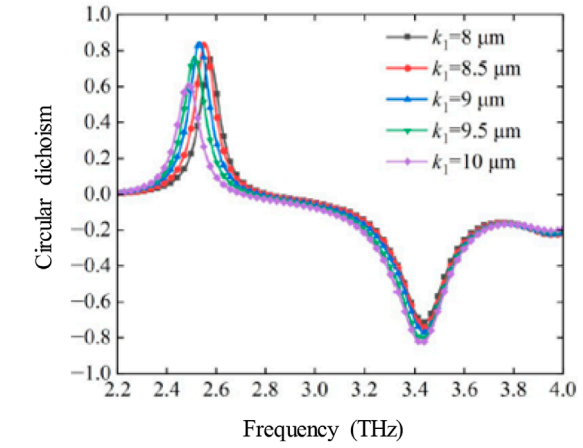

(a)

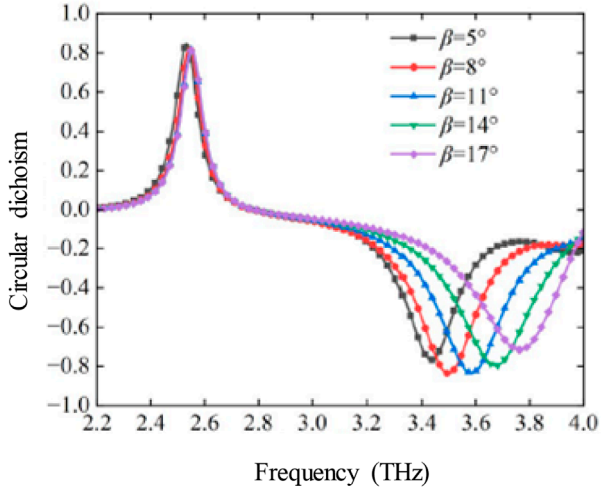

(b)

FIGURE 4
Impact of the structural parameters of meta-molecule units on dual-frequency circular dichroism. **(a)** Variation of low-frequency circular dichroism with k_1 **(b)** Variation of low-frequency circular dichroism with β.

2 Metasurface theoretical analysis

The dual-frequency THz circularly polarized wave absorption and abnormal reflection chiral metasurface array proposed in this paper can realize the control of the amplitude, phase, and polarization of circularly polarized waves in dual frequency bands [33–35]. The function is shown in Figure 1a. It absorbs the incident waves of LCP and RCP at the low frequency of 2.53 THz and high frequency of 3.43 THz, and realizes the chiral anomalous reflection of −26° and +19° for the orthogonal circularly polarized waves (low frequency and high frequency) in the 2 THz frequency bands. Figure 1b shows the top view and side view of the metasurface unit structure.

The unit is a metal-dielectric-metal "sandwich" structure [36–38]. The top pattern and the floor material are made of gold with a conductivity of 4.56×10^7 S/m and a thickness of 200 nm. The middle dielectric layer is made of polyimide with a dielectric constant of 3.5 and a loss tangent of 0.0027 [28]. The unit can be regarded as a meta-molecule composed of a meta-atom I and a meta-atom II with a period of p. Among them, the meta-atom I is a chiral rectangular resonant ring with asymmetric openings on the top and bottom [37, 38]. The Meta-atom II is a chiral circular resonant ring with openings at different angles on the top and bottom. The nested meta-molecule is a two-dimensional chiral structure with neither rotational symmetry nor mirror symmetry.

The specific values of the unit size parameters are shown in Table 1.

According to the theory of rotation-selective absorption and reflection [29], the Jones matrix is used to evaluate the circular dichroism of a two-dimensional chiral metasurface unit [39–41]. The connection between a linearly polarized electromagnetic wave's incident and reflected electric fields in the Cartesian coordinate system can be written as in Equation 1:

$$\begin{bmatrix} E_R^x \\ E_R^y \end{bmatrix} = \begin{bmatrix} r_{xx} & r_{xy} \\ r_{yx} & r_{yy} \end{bmatrix} \begin{bmatrix} E_I^x \\ E_I^y \end{bmatrix} = R \begin{bmatrix} E_I^x \\ E_I^y \end{bmatrix} \tag{1}$$

Among them, the reflected and incident electric fields are denoted by the letters E_R and E_I, respectively. The reflection coefficient is denoted by r, and the linear polarization direction is denoted by its superscript and subscript, x and y [42–44]. The reflection coefficient makes up the reflection matrix R. The circular polarization basis reflection matrix R_{circ} is created by transforming the linear polarization basis reflection matrix R via matrix transformation which is expressed by Equation 2:

$$\begin{aligned} R_{circ} &= \begin{bmatrix} r_{LR} & r_{LL} \\ r_{RR} & r_{RL} \end{bmatrix} \\ &= \Lambda^{-1} R \Lambda \\ &= \frac{1}{2} \begin{bmatrix} r_{xx} + r_{yy} + i(r_{xy} - r_{yx}) & r_{xx} - r_{yy} - i(r_{xy} + r_{yx}) \\ r_{xx} - r_{yy} + i(r_{xy} + r_{yx}) & r_{xx} + r_{yy} - i(r_{xy} - r_{yx}) \end{bmatrix} \end{aligned} \tag{2}$$

Among them, $\Lambda = 1/\sqrt{2} \begin{bmatrix} 1 & 1 \\ i & -i \end{bmatrix}$ denotes the transformation matrix, r_{LL} and r_{RR} are the coefficients of the co-polarization reflection; r_{RL} and r_{LR} represents the coefficients of cross-polarization reflection [45–47]. The subscripts "L" and "R" represent left-hand circular polarization (LCP) and right-hand circular polarization (RCP) in the direction of the wave, respectively.

Due to the presence of the underlying metal, the absorption performance of the unit is only related to the reflected field [48–50]. Considering the cross-polarization of the chiral unit, the left-handed absorption coefficient ALCP and the right-handed absorption coefficient ARCP of the unit can be expressed as in Equations 3, 4:

$$A_{LCP} = 1 - |r_{LL}|^2 - |r_{RL}|^2 \tag{3}$$

$$A_{RCP} = 1 - |r_{RR}|^2 - |r_{LR}|^2 \tag{4}$$

Equations 3, 4 show that the key to achieving efficient wave absorption is to make the co-polarization and cross-polarization reflection coefficients close to 0 at the same time.

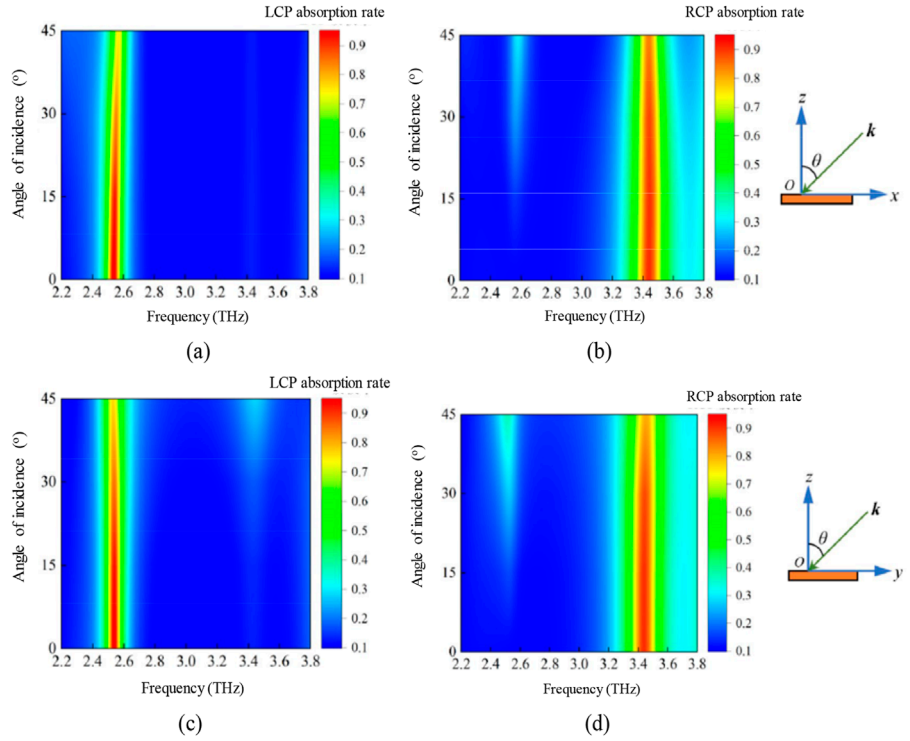

FIGURE 5
Absorption rate of the unit under two different azimuth oblique incidence. **(a)** LCP in *xOz* plane **(b)** RCP in *xOz* plane **(c)** LCP in *yOz* plane **(d)** RCP in *yOz* plane.

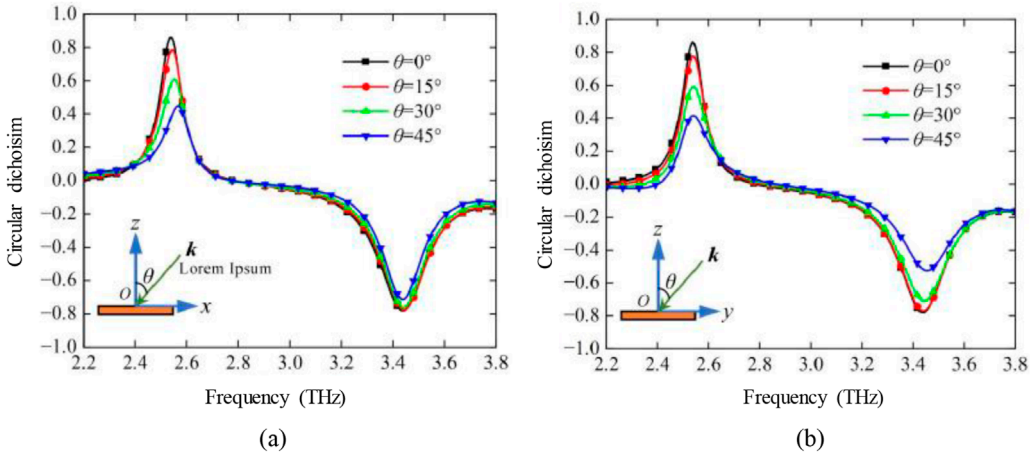

FIGURE 6
Circular dichroism of a metasurface unit cell under two different azimuth oblique incidence conditions. **(a)** CD in *xOz* plane **(b)** CD in *yOz* plane.

The difference between left-handed and right-handed wave absorption by a metasurface unit is measured by the circular dichroism (CD), which is defined in Equation 5:

$$CD = A_{LCP} - A_{RCP} \tag{5}$$

The value of CD can be positive or negative, indicating the selective absorption of the rotation direction of LCP waves or RCP waves.

3 Performance evaluation of unit circular polarization absorption

The CST Microwave Studio simulator is used to analyze meta-atom I, meta-atom II and meta-molecule. These chiral unit structures' distinctive properties, including their circular dichroism, wave absorption rate, and reflection coefficient, are primarily determined [51–53]. Using vertically incident LCP and RCP waves

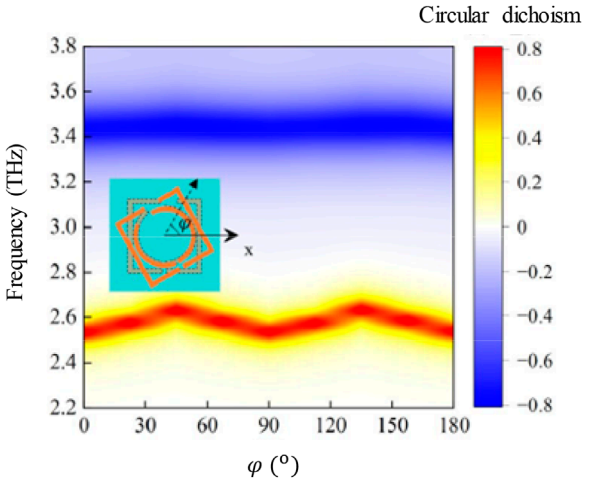

FIGURE 7
Effect of rotating unit pattern on circular dichroism.

as excitation, Figure 2 illustrates the simulation results of the reflection coefficient, wave absorption rate, and circular dichroism of the three structures. The results of Figures 2a,b show that, the meta-atom I can efficiently absorb LCP waves at 2.59 THz, while reflecting RCP waves and keeping their chirality unchanged. The absorption rate of LCP waves reaches 99.3%, while the absorption rate of RCP waves is only 8.6%, and the circular dichroism reaches 0.9 [54–56]. This is because meta-atom I can achieve cross-polarization reflection below 0.3 and co-polarization reflection above 0.9 in the frequency band of 2.4~3.8 THz, and resonate at 2.59 THz, making r_{LL} close to 0. The results of Figures 2c,d show that at 3.49 THz, the absorption rate of the meta-atom II for RCP wave is 54.6%, the absorption rate for LCP wave is 17.1%, and the circular dichroism is −0.37.

The excellent cross-polarization suppression performance of meta-atom I in a wide frequency band provides space for expanding the second chiral resonance point. The characteristic size of meta-atom II can be reasonably optimized to make its chiral resonance frequency just near the frequency point with the strongest cross-polarization suppression of meta-atom I, thereby realizing dual-frequency circular dichroism recombination [57–59]. Figures 2e, f show the performance of the meta-molecule after recombination. At the two frequencies of 2.53 THz and 3.43 THz, the meta-molecule has strong chiral absorption for LCP waves and RCP waves, respectively, and can achieve efficient chiral reflection for circularly polarized waves of the other hand direction. At 2.53 THz, the absorption rate of the meta-molecule for LCP waves is 96.3%, and the absorption rate for RCP waves is only 11.2%, and the circular dichroism reaches 0.85. The absorption rate of the meta-molecule for LCP waves is 14.1% at 3.43 THz. The absorption rate for RCP waves is 90.9%. The circular dichroism is −0.77. That is to say, the meta-molecule achieves opposite strong circular dichroism in two frequency bands [60–62]. It is possible to determine from observation that the meta-molecule's two chiral resonance frequency points are near to those of meta-atoms I and II.

The simulation results in Figure 2 show that the design scheme integrating two chiral resonant rings can improve the high-frequency chiral resonant response of meta-atom II while inheriting the low-frequency strong circular dichroism of meta-atom I. The reason is that the introduction of a chiral rectangular ring outside the chiral circular ring can significantly enhance the chiral characteristics of the structure and strengthen the coupling effect between adjacent metal structures.

To further evaluate the physical mechanism of chiral wave absorption of meta-molecular units, the surface current distribution of metamolecular units at 2.53 THz and 3.43 THz is simulated [63–65]. Figure 3 shows the surface current distribution of the unit at two resonance points when the LCP/RCP wave is incident.

As shown in Figures 3a,b, the LCP wave will excite a pair of antiparallel currents with approximately equal amplitudes on both sides of the rectangular ring at 2.53 THz. A magnetic moment perpendicular to the metasurface unit is produced by the circular magnetic dipole formed by these two current oscillations. To achieve the absorption of the LCP wave, this magnetic dipole mode will bind electromagnetic energy on the unit surface. The electromagnetic energy will then be dissipated by the metal's ohmic loss effect and the polyimide medium's absorption effect. The RCP wave can be effectively reflected since it stimulates a weak current [66–68]. The results of Figures 3c,d show that at 3.43 THz, the RCP wave will excite a pair of strong currents flowing in opposite directions on the right side of the rectangular and circular rings. The circular magnetic dipole formed by it can also achieve strong absorption of the RCP wave, while the LCP wave can only excite a weak surface current, so it is efficiently reflected.

The impact of the geometric parameters of the metasurface unit on the circular dichroism is shown in Figure 4. According to the analysis of the results of Figures 2, 3, the characteristic sizes of meta-atom I and meta-atom II can be adjusted respectively to achieve independent manipulation of the low-frequency and high-frequency circular dichroism working frequencies [69–71]. The results of Figure 4a show that when the size parameter k_1 changes in the range of 8~10 μm, the low-frequency circular dichroism of the meta-molecule always maintains a strong circular dichroism characteristic higher than 0.6, and the low-frequency chiral resonance frequency can be adjusted in the range of 2.48~2.58 THz. The high-frequency circular dichroism of the unit is almost unaffected by the size parameter k_1. The results in Figure 4b show that when the size parameter β increases from 5° to 17°, the high-frequency of chiral meta-molecule can be adjusted between 3.43 and 3.76 THz, and always maintains a strong circular dichroism higher than −0.7, and the low-frequency circular dichroism of the unit is almost unaffected by the size parameter β. Furthermore, the scaling method may be used to modify the structural size of the unit while controlling the two chiral resonance spots to broaden the spectrum, in accordance with the scalability of Maxwell's equations.

Figure 5 shows the absorption rates of LCP and RCP of the metasurface unit under different incident angles θ [72]. Because the designed metasurface unit is an anisotropic structure, the situation will be different at different azimuth angles of oblique incidence. Therefore, this paper studies the two oblique incidence situations when the wave vector is restricted to the xOz plane and the yOz plane. When the wave vector is restricted to the xOz plane, it can be seen from Figure 5a that as the incident angle θ increases to 45°, the LCP absorption rate remains at 74.4%, accompanied by a slight blue shift phenomenon [73]. In Figure 5b, the RCP absorption peak

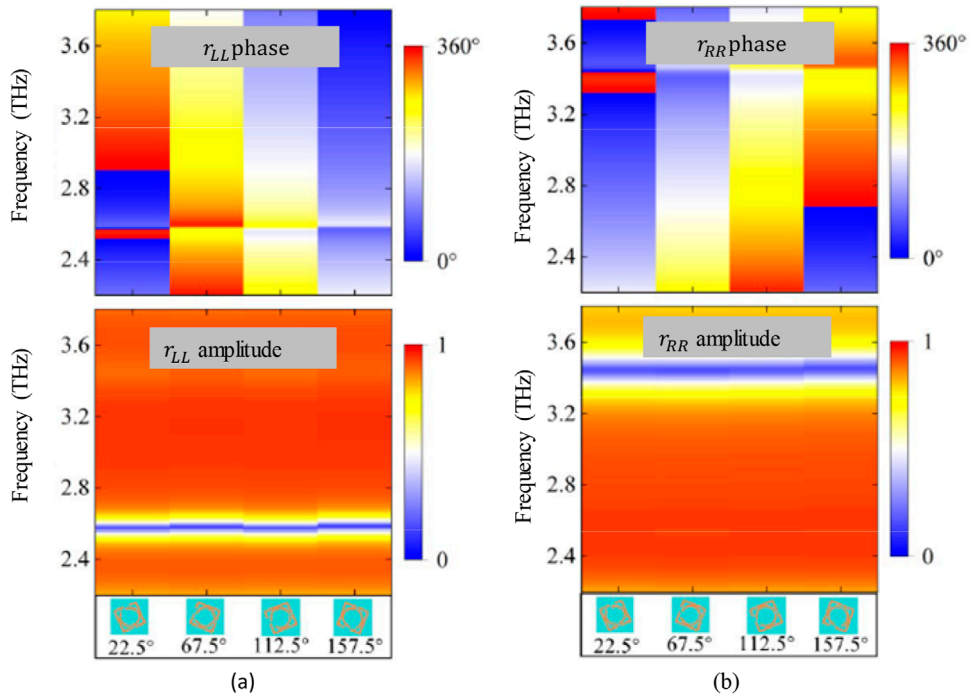

FIGURE 8
Phase and amplitude of co-polarization reflection coefficient of geometric phase metasurface encoding unit. **(a)** Four unit r_{LL} phase and amplitude **(b)** Four unit r_{RR} phase and amplitude.

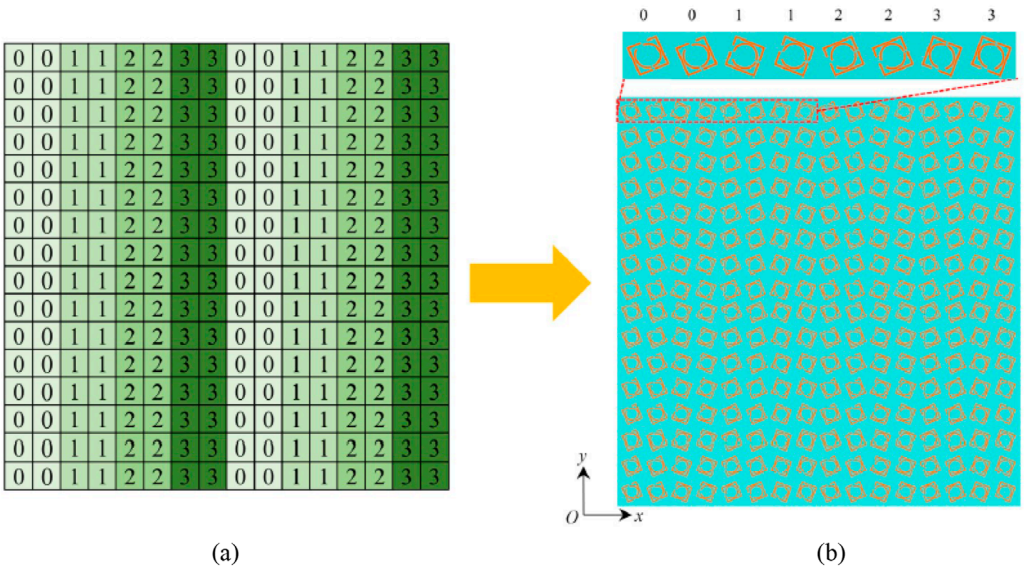

FIGURE 9
Schematic diagram of the coding arrangement of circular polarization absorption and anomalous reflection chiral metasurface array. **(a)** Gradient phase encoding strategy **(b)** 16 × 16 metasurface array.

hardly changes with the increase of the incident angle θ, and still has an RCP absorption rate of 83.9% when θ increases to 45°.

When the wave vector is limited to the yOz plane, the results of Figure 5c show that when θ is increased to 45°, the absorption rate of the unit to LCP waves is 76.1%. The results of Figure 5d show that when the RCP absorption peak increases with the incident angle θ to 45°, the absorption rate of the unit to RCP is greater than 80.1%.

It should be noted that when the wave vector is limited to the x-z plane, the unit will produce an RCP absorption band of approximately 28% near 2.6 THz when θ is close to 45°. The frequency of this RCP

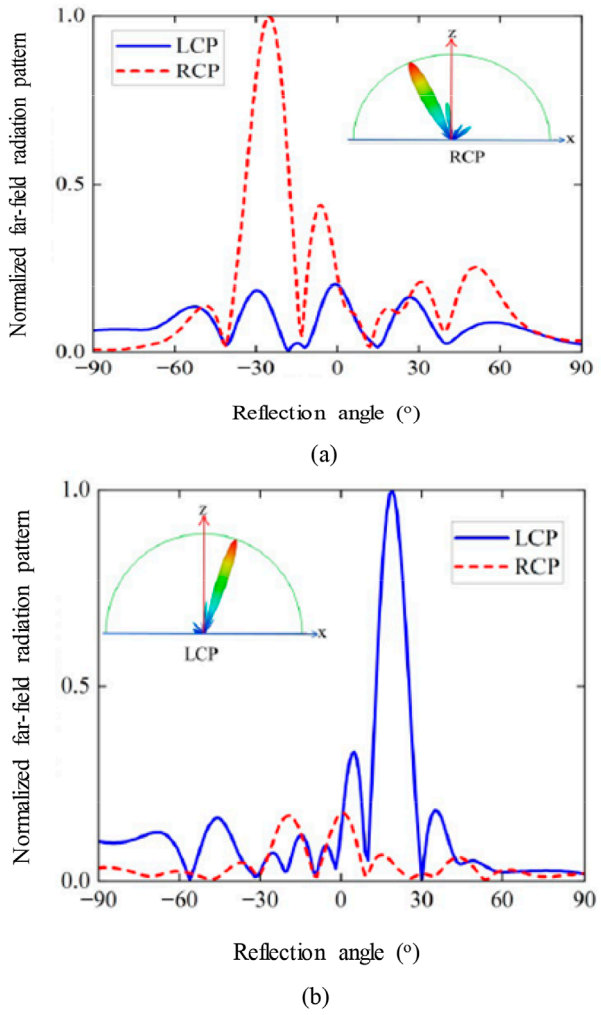

FIGURE 10
Normalized far-field pattern of coded chiral metasurface array. **(a)** 2.53 THz **(b)** 3.43 THz.

absorption band is close to the frequency of the LCP absorption band, which will affect the CD of the unit considering this oblique incidence condition. Figure 6a intuitively shows this influence. As the incident angle θ in the x-z plane increases, the circular dichroism of the unit at 2.53 THz is weakened and blue-shifted. When θ = 45°, the circular dichroism will be reduced to 0.45. The circular dichroism of the unit near 3.43 THz is less affected by the incident angle, the operating frequency is almost not shifted, and it still has a strong circular dichroism of −0.72 when θ = 45° [74]. When the wave vector is confined to the yOz plane, the asymmetry of the unit structure is more reduced compared with the first oblique incidence case, so the performance of circular dichroism deteriorates more seriously. The results in Figure 6b show that when the incident angle θ in the yOz plane increases to 45°, the dual-frequency circular dichroism of the unit will drop to 0.42 and −0.51 respectively. Therefore, the hand-selective absorption performance of the structure under this oblique incidence is not stable, and this problem needs to be paid attention to in practical applications.

Figure 7 shows the relationship between the circular dichroism of the unit and the simulation frequency, and the inset is an illustration of the rotation angle φ of the pattern. As φ increases, the unit can still maintain the characteristics of having opposite strong circular dichroism at two frequency points [75]. The outer rectangular ring structure responsible for low-frequency circular dichroism has a strong coupling with the adjacent unit, and the working frequency of positive circular dichroism fluctuates periodically with φ in the range of 2.53~2.65 THz. The inner ring structure responsible for high-frequency negative circular dichroism has very little coupling with the adjacent unit, so for any rotation angle φ, the unit can maintain a strong circular dichroism of −0.77 at 3.43 THz.

4 Metasurface array design and performance evaluation

Only the unit rotation angle can govern the extra phase shift produced by the metasurface. According to theory, this phase control technique has a broad bandwidth [30], allowing the total rotation unit pattern to simultaneously control the dual-frequency reflection phase. In order to overcome the periodic change of the working frequency of the circular dichroism when the unit rotates, this paper selects four units with φ of 22.5°, 67.5°, 112.5° and 157.5° for separate simulation verification. The phase and amplitude of the co-polarization reflection coefficient of the four units are shown in Figure 8. At the two resonance points of 2.53 THz and 3.43 THz, as the rotation angle increases, the reflection phase of the four units appears to be faulted. This is because the chiral wave absorption characteristics of the unit at the resonance point blur the phase change.

The LCP wave's reflection phase progressively diminishes as the rotation angle grows at the non-resonant frequency, whereas the RCP wave's reflection phase gradually increases as the rotation angle increases [76–78]. The phase change trends are exactly opposite, and both can achieve a phase coverage of nearly 360°. Further observation also shows that the absolute value of the reflection phase difference between adjacent units is about 90°, which is exactly twice the rotation angle increment of 45°, and this phase change is dispersion-free, which conforms to the geometric phase theory. The co-polarization reflection amplitude of the four units is constant over the broad frequency range of 2.2~3.8 THz, and it has a greater reflection amplitude at the non-resonant point, according to the reflection coefficient's amplitude. Based on this excellent reflection coefficient dispersion-free performance, these four meta-molecular units can be used to design circularly polarized wave absorbing and abnormal reflection metasurface arrays.

For the above four meta-molecular units with a reflection phase difference of 90°, digital coding can be used to represent their phase response to design a reasonable coding strategy [31, 32]. This paper uses the numbers "0", "1", "2" and "3" to represent these four units, and uses the coding strategy of reflection phase gradient arrangement to construct a 2-bit strong circular dichroism circular polarization amplitude-phase control metasurface, in order to simultaneously realize the three functions of dual-frequency circular polarization chiral absorption, circular polarization conversion and abnormal reflection. The metasurface coding arrangement strategy is shown in Figure 9a. In the x direction, the four units form a superstructure unit cell with a period of $L = 8 \times p$ in the encoding mode of "00112233", and extend with a period of L in the x direction. In the y direction, the superstructure unit cell extends

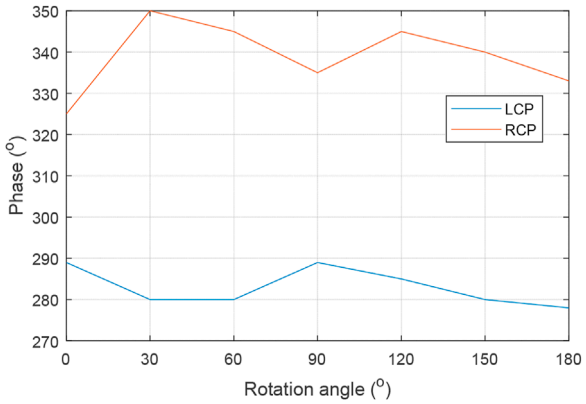

FIGURE 11
Variation of LCP and RCP phase angle with rotation angle.

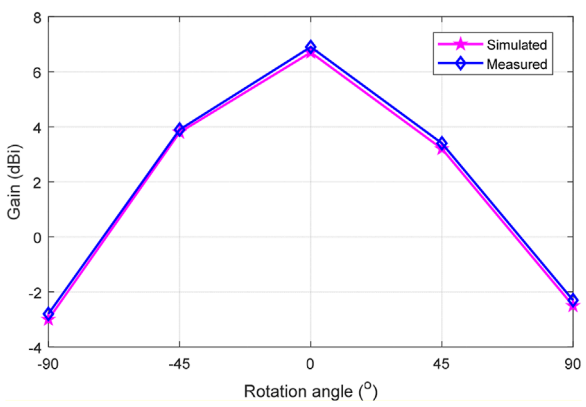

FIGURE 12
Simulated and measured gain comparison vs. rotation angle.

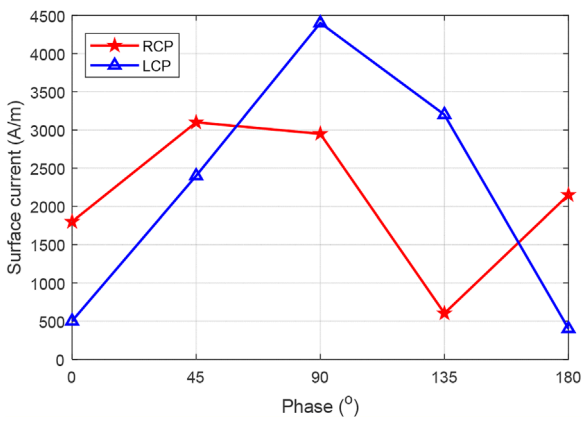

FIGURE 13
Surface current of LCP and RCP waves.

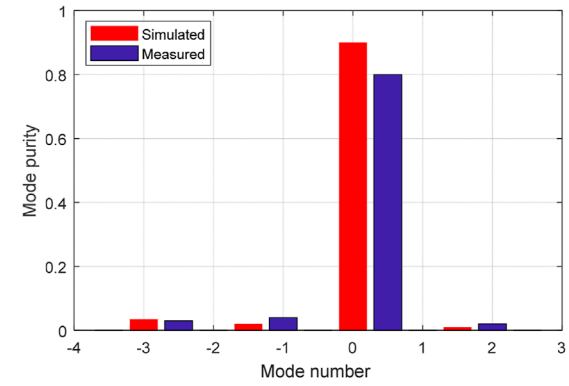

FIGURE 14
Comparison of simulated and measured comparison of mode purity (l = 0).

with a period of p. The final constructed 16 × 16 supersurface array is shown in Figure 9b.

The metasurface with gradient phase can change the reflection direction of electromagnetic waves, that is, realize the abnormal reflection of electromagnetic waves [79, 80]. The reflection angle θ_r of the abnormal reflection is obtained by the generalized form of Snell's law:

$$\theta_r = \pm \sin^{-1}[\sin\theta_i + \lambda_0/L] \quad (6)$$

where θ_i represents the angle of incidence, λ_0 is the wavelength of the signal, and L denotes the period length of the metastructure unit cell. In the proposed metasurface array, θ_i is fixed to 0° and L = 268 μm. The sign of the reflection angle is specified as follows: "+" for LCP waves and "−" for RCP waves. Using Equation 6, the theoretical LCP/RCP reflection angles at the two resonance points of 2.53 THz and 3.43 THz are calculated to be −26° and +19° respectively.

The full-wave simulation was performed by using LCP/RCP plane waves to excite the metasurface at vertical incidence. Figure 10 displays the metasurface array's one-dimensional normalized far-field pattern, with the three-dimensional far-field pattern inset. The RCP wave experiences hand-preserving anomalous reflection with a reflection angle of −26° at 2.53 THz, whereas the LCP wave is heavily absorbed. The LCP wave experiences hand-preserving anomalous reflection with a reflection angle of +19° at 3.43 THz, while the RCP wave is heavily absorbed. The experimental results are consistent with the theoretical analysis. The simulation results show that the metasurface array has two functions of circularly polarized chiral absorption and chiral anomalous reflection in two frequency bands, it is able to control the amplitude and phase of the CP waves at the same time.

The further validate the effectiveness of the proposed metasurface, Figure 11 compares the performance of the LCP and RCP wave in terms of phase angle. As can be seen from Figure 11, the phase angle variation is considerable for covering the desired spectrum.

Figure 12 compares the simulated and measured gain of the metasurface under increasing rotation angle.

As can be seen that, the simulated and measured gain are consistent and effective.

TABLE 2 Comparison of the proposed and existing metasurface performance.

Reference	Operating frequency	Absorption (%)	Circular dichroism peak	Function
[38]	Terahertz (single frequency)	97	0.87	Circular polarization absorber
[39]	Microwave (dual frequency)	95.18 (Low frequency) 91.77 (High frequency)	0.78 (Low frequency) 0.69 (High frequency)	Circular polarization absorber
[40]	Microwave (dual frequency)	92 (Low frequency) 94 (High frequency)	−0.79 (Low frequency) 0.75 (High frequency)	Circular polarization absorption + Abnormal reflection
[41]	Mid-infrared (dual frequency)	64 (Low frequency) 89 (High frequency)	0.40 (Low frequency) 0.58 (High frequency)	Circular polarization absorber
[42]	Microwave (dual-frequency)	91.45 (Low frequency) 89.74 (High frequency)	0.71 (Low frequency) 0.63 (High frequency)	Circular polarization absorber
[43]	Terahertz (single frequency)	92.86 (Low frequency) 88.76 (High frequency)	0.69 (Low frequency) 0.76 (High frequency)	Circular polarization absorber
[44]	Microwave (dual-frequency)	64.13 (Low frequency) 85.13 (High frequency)	0.52 (Low frequency) 0.65 (High frequency)	Circular polarization absorption + Abnormal reflection
Proposed	THz (dual frequency)	96.3 (Low frequency) 90.9 (High frequency)	0.85 (Low frequency) −0.77 (High frequency)	Circular polarization absorption + Abnormal reflection

Figure 13 evaluates the surface current of the RCP and LCP waves with different values of phase angles. As can be seen from Figure 13, asymmetric electric field is created to generate resonant phase delay between both sides of the metasurface.

Figure 14 compares the OAM mode purity performance. It can be seen from Figure 14, the mode purity level at desired mode number is higher which is desirable for designing the metasuface generating OAM waves. This also enables to generates waves at specific mode.

Table 2 lists the comparison between the proposed metasurface design the existing works. Currently, most THz chiral metasurfaces with strong circular dichroism can usually only work in a single frequency band. From Table 2, it is evident that the suggested metasurface offers benefits in dual-frequency circular dichroism peak and multifunctional integration in addition to extending the operating frequency range to two.

5 Conclusion

This paper uses Jones matrix theory and geometric phase control principle to design a dual-frequency THz circularly polarized wave absorption and abnormal reflection chiral metasurface array. The metasurface realizes opposite circular dichroism in 2 THz frequency bands. Compared with ordinary metal plates, it can perform hand-preserving reflection of circularly polarized waves of specific rotation direction and has good circular polarization conversion ability. At the same time, the proposed metaruface has the ability of geometric phase control, and can realize the abnormal reflection of circularly polarized waves at a given angle through gradient phase arrangement. It explains the circular polarization absorption mechanism of chiral metasurface units by analyzing the surface current distribution of metasurface units. Through phase gradient arrangement, a chiral metasurface integrated array with chiral absorption, polarization conversion and abnormal reflection functions is designed, which realizes the absorption of circularly polarized waves of specific rotation direction at two working frequencies, and makes the orthogonal circularly polarized waves have chiral-preserving abnormal reflections at −26° and +19° respectively. In the future, it will promote its application in THz energy collection, polarization conversion, sensing, imaging and other fields.

Data availability statement

The original contributions presented in the study are included in the article/supplementary material, further inquiries can be directed to the corresponding authors.

Author contributions

HM: Writing – original draft, Methodology, Writing – review and editing, Project administration, Resources, Validation, Conceptualization. SK: Validation, Formal Analysis, Data curation, Funding acquisition, Writing – review and editing, Software, Investigation, Writing – original draft, Resources. RZ: Visualization, Data curation, Writing – original draft, Funding acquisition, Conceptualization, Project administration, Validation,

Investigation, Writing – review and editing, Supervision. RS-D: Writing – original draft, Methodology, Project administration, Visualization, Software, Resources, Validation, Writing – review and editing, Funding acquisition, Conceptualization, Supervision. JE-G: Methodology, Data curation, Funding acquisition, Investigation, Writing – original draft, Resources, Conceptualization, Validation, Writing – review and editing, Formal Analysis. DA: Writing – original draft, Resources, Visualization, Software, Formal Analysis, Writing – review and editing, Conceptualization, Validation, Methodology.

Funding

The author(s) declare that financial support was received for the research and/or publication of this article. Princess Nourah bint Abdulrahman University Researchers Supporting Project number (PNURSP2025R140), Princess Nourah bint Abdulrahman University, Riyadh, Saudi Arabia. RZ would like to acknowledge Universiti Malaya Research Excellence Grant 2/2024 (Project No. UMREG038-2024).

Conflict of interest

The authors declare that the research was conducted in the absence of any commercial or financial relationships that could be construed as a potential conflict of interest.

Generative AI statement

The author(s) declare that no Generative AI was used in the creation of this manuscript.

Publisher's note

References

1. Chen Z, Guan S, Xie Q, Li Z, Gao Z, Negahban M. Locally resonant metasurface for low-frequency transmissive underwater acoustic waves. *Front Phys* (2023) 10:1098261–6. doi:10.3389/fphy.2022.1098261

2. Shen S, Liu X, Shen Y, Qu J, Pickwell-MacPherson E, Wei X, et al. Recent advances in the development of materials for terahertz metamaterial sensing. *Adv Opt Mater* (2022) 10(1):2101008–14. doi:10.1002/adom.202101008

3. Tao X, Qi L, Yang J, Uqaili J, Lan F, Yang Z. Bifunctional terahertz metasurface for transmissive broadband linear-to-circular and linear polarization. *IEEE Trans Terahertz Sci Technology* (2023) 13(3):254–61. doi:10.1109/TTHZ.2023.3250943

4. Born B, Lee S, Song J, Lee J, Ko W, Brongersma M. Off-axis metasurfaces for folded flat optics. *Nat Commun* (2023) 14(5602):5602–18. doi:10.1038/s41467-023-41123-x

5. Su J, Chen G, Ma C, Zhang Q, Li X, Geng Y, et al. A metastructure based on amorphous carbon for high efficiency and selective solar absorption. *Nanomaterials* (2024) 14(7):580–15. doi:10.3390/nano14070580

6. Lin H, Zou Y, Wu Y, Wang X, Zhu H, Zhang X, et al. Broadband terahertz metamaterial absorber with a tunable performance based on vanadium dioxide. *Appl Phys A* (2023) 129:565–15. doi:10.1007/s00339-023-06842-4

7. Dong L, Si M, Xu H, Shen Q, Lv X, Zhuang Y, et al. Rapid customized design of a conformal optical transparent metamaterial absorber based on the circuit analog optimization method. *Opt Express* (2022) 30(5):8303–15. doi:10.1364/oe.452694

8. Chen W, Liu Y, Zhang C, He J, Zhang Y. Metasurface-based wide-angle reflective metalens with consistently constant focusing efficiency. *Infrared Phys and Technology* (2024) 139:105341–14. doi:10.1016/j.infrared.2024.105341

9. Chen D, Zeng H, Huang Q, Su L, Dou Y, Cheng K, et al. Composite control of wavelength and polarization of a metalens based on double-layer geometric phase. *Phys Lett A* (2025) 535:130283–13. doi:10.1016/j.physleta.2025.130283

10. Zhang Y, Luan W, Yan X, Gao X, Zeng X, Jin X, et al. Ultra-braodband asymmetric transmission and linear polarization conversion based on terahertz metamaterials. *Appl Phys B* (2022) 128(156):1–12. doi:10.1007/s00340-022-07871-2

11. Stephen L, Yogesh N, Subramanian V. Broadband asymmetric transmission of linearly polarized electromagnetic waves based on chiral metamaterial. *J Appl Phys* (2018) 123(3):033103–16. doi:10.1063/1.5008614

12. Cheng G, Si M, Tang P, Zhang Q, Lv X. Study of symmetries of chiral metasurfaces for azimuth-rotation-independent cross polarization conversion. *Opt Express* (2022) 30(4):5722–15. doi:10.1364/oe.452773

13. Zhu G, Bai Z, Chen J, Huang C, Wu L, Fu C, et al. Ultra-dense perfect optical orbital angular momentum multiplexed holography. *Opt Express* (2021) 29(18):28452–60. doi:10.1364/oe.430882

14. Abbas R, Luo J, Qi X, Naz A, Khan I, Liu H, et al. Silver nanoparticles: synthesis, structure, properties and applications. *Nanomaterials* (2024) 14(17):1425–13. doi:10.3390/nano14171425

15. Huang Y, Xie X, Pu M, Guo Y, Xu M, Ma X, et al. Dual-functional metasurface toward giant linear and circular dichoism. *Adv Opt Mater* (2020) 8(11):1–15. doi:10.1002/adom.201902061

16. Liu M, Plum E, Li H, Li S, Xu Q, Zhang X, et al. Temperature-controlled optical activity and negative refractive index. *Adv Funct Mater* (2021) 31(14):2010249–261. doi:10.1002/adfm.202010249

17. Cai H, Gu L, Hu H, Zhan Q. Enhancement methods for chiral optical signals by tailoring optical fields and nanostructures. *Engineering* (2025) 45:25–43. doi:10.1016/j.eng.2024.12.022

18. Tan X, Lin J, Xu K, Chen P, Ma L, Lau R. Mirror detection with the visual chirality cue. *IEEE Trans Pattern Anal Machine Intelligence* (2022) 45(3):3492–504. doi:10.1109/TPAMI.2022.3181030

19. Qu Y, Lei L, Yu Y, Zhang X, Qian Z Coexistence of circular dichoism and asymmetric transmission in Babinet-complementary metamaterials. *Opt Express* (2022) 30(17):1–15. doi:10.1364/OE.464798

20. Liu Z, Xu Y, Ji C, Chen S, Li X, Zhang X, et al. Fano-enhanced circular dichoism in deformable stereo metasurfaces. *Adv Mater* (2020) 32(8):1–14. doi:10.1002/adma.201907077

21. Frese D, Wei Q, Wang Y, Huang L, Zentgraf T Nanoreciprocal asymmetric polarization encryption by layered plasmonic metasurfaces. *Nano Lett* (2019) 19(6):3976–80. doi:10.1021/acs.nanolett.9b01298

22. Huang Y, Xiao T, Xie Z, Zheng J, Su Y, Chen W, et al. Single-layered reflective metasurface achieving simultaneous spin-selective perfect absorption and efficient wavefront manipulation. *Adv Opt Mater* (2021) 9(5):2001663–14. doi:10.1002/adom.202001663

23. Xie Y, Yang C, Wang Y, Shen Y, Deng X, Zhou B, et al. Anomalous refraction and reflection characteristics of bend V-shaped antenna metasurfaces. *Scientific Rep* (2019) 9:6700–13. doi:10.1038/s41598-019-43138-1

24. Su D, Wang X, Shang G, Ding X, Burokur S, Liu J, et al. Amplitude-phase modulation metasurface hologram with inverse angular spectrum diffraction theory. *J Phys D: Appl Phys* (2022) 55(23):235102–15. doi:10.1088/1361-6463/ac5699

25. Wang Z, Yao Y, Pan W, Zhou H, Chen Y, Lin J, et al. Bifunctional manipulation of terahertz waves with high-efficiency transmissive dielectric metasurfaces. *Adv Sci* (2023) 10(4):2205499–15. doi:10.1002/advs.202205499

26. Sheng L, Chen Y, Yuan S, Liu X, Zhang Z, Jing H, et al. Photonic spin hall effect: physics, manipulations, and applications. *Prog Quan Electronics* (2023) 92:100484–13. doi:10.1016/j.pquantelec.2023.100484

27. Penarrubia A, Teniente J, Kuznetsov S, Orazbayev B, Beruete M. Ultrathin and high-efficiency pancharatnam-berry phase metalens for millimeter waves. *Appl Phys Lett* (2021) 118:1–16. doi:10.1063/5.0048907

28. Bhattacharjee P. The generalized vectorial laws of reflection and refraction leading to the development of novel equations involving the coordinates of the source point, point of observation, and the point of incidence. *Optik* (2020) 218:164988–15. doi:10.1016/j.ijleo.2020.164988

29. Meng Z, Shi Y, Wei W, Zhang Y, Li L. Graphene-based metamaterial transmitarray antenna design for the generation of tunable orbital angular momentum vortex electromagnetic waves. *Opt Mater Express* (2019) 9(9):3709–16. doi:10.1364/OME.9.003709

30. Wang L, Yang Y, Li S, Deng L, Hong W, Zhang C, et al. Terahertz reconfigurable metasurface for dynamic non-diffractive orbital angular momentum beams using vanadium dioxide. *IEEE Photon J* (2020) 12(3):1–12. doi:10.1109/JPHOT.2020.3000779

31. Wang L, Yang Y, Deng L, Hong W, Zhang C, Li S. Vanadium dioxide embedded frequency reconfigurable metasurface for multi-dimensional multiplexing of terahertz communication. *J Phys D: Appl Phys* (2021) 54(25):255003. doi:10.1088/1361-6463/abf166

32. Yang Q, Wang Y, Liang L, Yang M. Broadband transparent terahertz vortex beam generator based on thermally tunable geometric metasurface. *Opt Mater* (2021) 121:111574. doi:10.1016/j.optmat.2021.111574

33. Yu J, Lang T, Chen H. All-metal terahertz metamaterial absorber and refractive index sensing performance. *Photonics* (2021) 8(5):164–13. doi:10.3390/photonics8050164

34. Li C, Liao Y, Bikbaev R, Yang J, Chen L, Maksimov DN, et al. Selective plasmonic responses of chiral metamirrors. *Nanomaterials* (2024) 14(21):1705–14. doi:10.3390/nano14211705

35. Zhou X, Yang H, Zhao R, Fu Y, Yang Y, Zhou X, et al. Dual-band chiral metasurface for spin-selective absorption and temperature-induced electromagnetic chameleon. *Appl Surf Sci* (2025) 682:161666–15. doi:10.1016/j.apsusc.2024.161666

36. Wang L, Lan F, Zhang Y, Liang S, Liu W, Yang Z, et al. A fractional phase-coding strategy for terahertz beam patterning on digital metasurfaces. *Opt Express* (2020) 28(5):6395–15. doi:10.1364/oe.385691

37. Hu S, Li M, Xu J, Zhang H, Zhang S, Cui T, et al. Electromagnetic metamaterial agent. *Light: Sci and Appl* (2025) 14(12):12–8. doi:10.1038/s41377-024-01678-w

38. Cui Y, Wang X, Jiang H, Jiang Y. High-efficiency and tunable circular dichoism in chiral graphene metasurface. *J Phys D: Appl Phys* (2022) 55(13):1–13. doi:10.1088/1361-6463/ac4450

39. Wang L, Huang X, Li M, Dong J. Chirality selective metamaterial absorber with dual bands. *Opt Express* (2019) 27(18):25983–14. doi:10.1364/oe.27.025983

40. Guo Y, Ma H, Wang Z, Wu L, Wu R, Cui T Dual-band chiral metasurface for independent control of spin-selective reflections. *Opt Express* (2022) 30(8):1–14. doi:10.1364/OE.453703

41. Tang H, Rosenmann D, Czaplewski D, Yang X, Gao J Dual-band selective circular dichoism in mid-infrared chiral metasurfaces. *Opt Express* (2022) 30(11):1–11. doi:10.1364/OE.457218

42. Wang Y, Wang Y, Yu A, Hu M, Wang Q, Pang C, et al. Non-interleaved shared-aperture full-stokes metalens *via* prior-knowledge-driven inverse design. *Adv Mater* (2025) 37(8):2408978. doi:10.1002/adma.202408978

43. Zheng J, Sun J, Liu F, Liu X, Peng J, Zhang J, et al. Flight verification of cooling self-sustaining high-temperature superconducting motor. *Superconductor Sci Technology* (2024) 37(7):07LT02. doi:10.1088/1361-6668/ad54f5

44. Zhou G, Huang J, Li H, Li Y, Jia G, Song N, et al. Multispectral camouflage and radiative cooling using dynamically tunable metasurface. *Opt Express* (2024) 32(7):12926–40. doi:10.1364/OE.517889

45. Zhou YJ, Wu XB, Cai XD, Xu HX, Li QY, Xiong W, et al. Smart meta-device powered by stray microwave energies: a green approach to shielding external interference and detection. *Appl Energy* (2025) 378:124770. doi:10.1016/j.apenergy.2024.124770

46. Zhang X, Zhang H, Liu L, Han Z, Poor HV, Di B. Target detection and positioning aided by reconfigurable surfaces: reflective or holographic? *IEEE Trans Wireless Commun* (2024) 23(12):19215–30. doi:10.1109/TWC.2024.3480353

47. Ma P, Yao T, Liu W, Pan Z, Chen Y, Yang H, et al. A 7-kW narrow-linewidth fiber amplifier assisted by optimizing the refractive index of the large-mode-area active fiber. *High Power Laser Sci Eng* (2024) 12:e67. doi:10.1017/hpl.2024.41

48. Hongyun C, Mengyao Y, Xue P, Ge X. Joint active and passive beamforming design for hybrid RIS-aided integrated sensing and communication. *China Commun* (2024) 21(10):1–12. doi:10.23919/JCC.ja.2023-0213

49. Pei H, Pang H, Quan W, Fan W, Yuan L, Zhang K, et al. Pulsed optical pumping in electron spin vapor. *Measurement* (2024) 231:114619. doi:10.1016/j.measurement.2024.114619

50. Sun J, Zhou S, Lin Q. A high-precision and fast modeling method for amplifiers. *Int J Numer Model Electron Networks, Devices Fields* (2025) 38(2):e70051. doi:10.1002/jnm.70051

51. Sun J, Zhou S (2025). Cuckoo search-ExtraTrees model for Radio-frequency power amplifier under different temperatures. *arXiv* 79, 433–8. doi:10.1515/freq-2024-0298

52. Wang Q, Luo R, Wang Y, Fang W, Jiang L, Liu Y, et al. Set/reset bilaterally controllable resistance switching Ga-doped Ge2Sb2Te5 long-term electronic synapses for neuromorphic computing. *Adv Funct Mater* (2023) 33(19):2213296. doi:10.1002/adfm.202213296

53. Zhang Y, Gang Y, Wu P, Fan G, Xu W, Ai B, et al. Integrated sensing, communication, and computation in SAGIN: joint beamforming and resource allocation. *IEEE Trans Cogn Commun Networking* (2025) 1. doi:10.1109/TCCN.2025.3577377

54. Li P, Li R, Fan Z, Han J, Ding G, Wang Q, et al. 3D printed high-temperature ceramic conformal array antenna: design, analysis, manufacturing, and testing. *Defence Technology* (2025). doi:10.1016/j.dt.2025.05.012

55. Ren Z, Yang Z, Mu W, Liu T, Liu X, Wang Q. Ultra-broadband perfect absorbers based on biomimetic metamaterials with dual coupling gradient resonators. *Adv Mater* (2025) 37(11):2416314. doi:10.1002/adma.202416314

56. Niu S, Liu X, Wang C, Mu W, Xu W, Wang Q. Breaking the trade-off between complexity and absorbing performance in metamaterials through intelligent design. *Small* (2025) 21:2502828. doi:10.1002/smll.202502828

57. Yang Y, Zhang Z, Zhou Y, Wang C, Zhu H. Design of a simultaneous information and power transfer system based on a modulating feature of magnetron. *IEEE Trans Microwave Theor Tech* (2023) 71(2):907–15. doi:10.1109/TMTT.2022.3205612

58. Zhang H, Xu Y, Luo R, Mao Y. Fast GNSS acquisition algorithm based on SFFT with high noise immunity. *China Commun* (2023) 20(5):70–83. doi:10.23919/JCC.2023.00.006

59. Bai X, Xiao Z, Shi H, Zhang K, Luo Z, Wu Y. Omnidirectional sound wave absorption based on the multi-oriented acoustic meta-materials. *Appl Acoust* (2025) 228:110344. doi:10.1016/j.apacoust.2024.110344

60. Guan Y, Yang L, Chen C, Wan R, Guo C, Wang P. Regulable crack patterns for the fabrication of high-performance transparent EMI shielding windows. *iScience* (2025) 28(1):111543. doi:10.1016/j.isci.2024.111543

61. Zhao Y, Xing S, Jin Q, Yang N, He Y, Zhang J. Excellent angular and electrical performance damage tolerance of wave-absorbing laminate *via* gradient A-T-A design. *Composites Commun* (2024) 46:101838. doi:10.1016/j.coco.2024.101838

62. Deng S, Wu L, Shi G, Xing L, Jian M, Xiang Y, et al. Learning to compose diversified prompts for image emotion classification. *Comput Vis Media* (2024) 10(6):1169–83. doi:10.1007/s41095-023-0389-6

63. Shi G, Deng S, Wang B, Feng C, Zhuang Y, Wang X. One for all: a unified generative framework for image emotion classification. *IEEE Trans Circuits Syst Video Technology* (2024) 34(8):7057–68. doi:10.1109/TCSVT.2023.3341840

64. Zheng Y, Zheng J, Wang X, Lu Y. Gamma radiation effects on high-temperature superconducting ReBCO tape. *Superconductor Sci Technology* (2024) 37(4):045013. doi:10.1088/1361-6668/ad2fda

65. Shi H, Dao SD, Cai J. LLMFormer: large language model for open-vocabulary semantic segmentation. *Int J Computer Vis* (2025) 133(2):742–59. doi:10.1007/s11263-024-02171-y

66. Wang Z, Zhang C, Chen Z, Hu W, Lu K, Ge L, et al. ACR-Net: learning high-accuracy optical flow *via* adaptive-aware correlation recurrent network. *IEEE Trans Circuits Syst Video Technology* (2024) 34:9064–77. doi:10.1109/TCSVT.2024.3395636

67. Li X, Lu Z, Yuan M, Liu W, Wang F, Yu Y, et al. Tradeoff of code estimation error rate and terminal gain in SCER attack. *IEEE Trans Instrumentation Meas* (2024) 73:1–12. doi:10.1109/TIM.2024.3406807

68. Wang X, Chen X, He Q, Hui Y, Xu C, Wang B, et al. Bidirectional, multilayer MXene/Polyimide aerogels for ultra-broadband microwave absorption. *Adv Mater* (2024) 36(36):2401733. doi:10.1002/adma.202401733

69. Wang X, Chen X, Wang B, He Q, Cao J, Zhu Y, et al. Ultra-bandwidth microwave absorption and low angle sensitivity in dual-network aerogels with dual-scale pores. *Small* (2025) 21:2412744. doi:10.1002/smll.202412744

70. Wang Z, He G, Wang Y, Fan J, Zhang Y, Chai Y, et al. Wave propagation in finite discrete chains unravelled by virtual measurement of dispersion properties. *IET Sci Meas and Technology* (2024) 18(6):280–8. doi:10.1049/smt2.12193

71. Li D, Li P, Zhao J, Liang J, Liu J, Liu G, et al. Ground-to-UAV sub-terahertz channel measurement and modeling. *Opt Express* (2024) 32(18):32482–94. doi:10.1364/OE.534369

72. Chen S, Jiang H, Hu J, Zheng T, Wang M, Xiao Z, et al. Echoes of fingertip: unveiling POS terminal passwords through Wi-Fi beamforming feedback. *IEEE Trans Mobile Comput* (2025) 24(2):662–76. doi:10.1109/TMC.2024.3465564

73. Deng J, Gao N, Chen X. Ultrawide attenuation bands in gradient metabeams with acoustic black hole pillars. *Thin-Walled Structures* (2023) 184:110459. doi:10.1016/j.tws.2022.110459

74. Deng J, Gao N. Broadband vibroacoustic reduction for a circular beam coupled with a curved acoustic black hole *via* nullspace method. *Int J Mech Sci* (2022) 233:107641. doi:10.1016/j.ijmecsci.2022.107641

75. Gao N, Zhang Z, Liang X, Li Y, Pan G. Broadband multi-unit composite metamaterial for simultaneous sound wave and electromagnetic

wave absorption. *Mater and Des* (2025) 251:113671. doi:10.1016/j.matdes.2025.113671

76. Yang Z, Huo S, Zhang Z, Meng F, Liu B, Wang Y, et al. High-precision multibit opto-electronic synapses based on ReS2/h-BN/Graphene heterostructure for energy-efficient and high-accuracy neuromorphic computing. *Adv Funct Mater* (2025):2509119. doi:10.1002/adfm.202509119

77. Xu H, Wei H, Chen H, Chen Z, Zhou X, Xu H, et al. Effect of periodic phase modulation on the matched filtering with insufficient phase-shift capability. *IEEE Trans Aerospace Electron Syst* (2025) 61(3):5755–70. doi:10.1109/TAES.2024.3520959

78. Xu H, Zhang Y, Chen Z, Pan Q, Quan Y. An optimization-based deconvolution approach for recovering time-varying phase modulation signal of metasurface. *IEEE Trans Antennas Propagation* (2025) 1. doi:10.1109/TAP.2025.3567818

79. Fan S, Han C, He K, Bai L, Chen L, Shi H, et al. Acoustic moiré flat bands in twisted heterobilayer metasurface. *Adv Mater* (2025) 37:2418839. doi:10.1002/adma.202418839

80. Fu M, Ma Z, Gao C, Ye Y, Li W, Hou D, et al. A multi-functional VOC sensor based on cascaded quartz crystal resonators. *IEEE Electron Device Lett* (2025) 46(3):476–9. doi:10.1109/LED.2025.3528024